

# Monitoring simultaneously the growth of nanoparticles and aggregates by *in situ* ultra-small-angle x-ray scattering

Hendrik K. Kammler<sup>a)</sup> and Gregory Beaucage<sup>b),c)</sup>

Particle Technology Laboratory, Department of Mechanical and Process Engineering, ETH Zurich, ML F23, CH-8092 Zürich, Switzerland

Douglas J. Kohls and Nikhil Agashe

Department of Chemical and Materials Engineering, University of Cincinnati, 540 Engineering Research Center, Cincinnati, Ohio 45221-0012

Jan Ilavsky

UNICAT, Advanced Photon Source, Building 438D, 9700 South Cass Avenue, Argonne National Laboratory, Argonne, Illinois 60439

(Received 5 April 2004; accepted 13 December 2004; published online 15 February 2005)

Ultra-small-angle x-ray scattering can provide information about primary particles and aggregates from a single scattering experiment. This technique is applied *in situ* to flame aerosol reactors for monitoring simultaneously the primary particle and aggregate growth dynamics of oxide nanoparticles in a flame. This was enabled through the use of a third generation synchrotron source (Advanced Photon Source, Argonne IL, USA) using specialized scattering instrumentation at the UNICAT facility which is capable of simultaneously measuring nanoscales to microscales (1 nm to 1  $\mu\text{m}$ ). More specifically, the evolution of primary-particle diameter, mass-fractal dimension, geometric standard deviation, silica volume fraction, number concentration, radius of gyration of the aggregate, and number of primary particles per aggregate are measured along the flame axis for two different premixed flames. All these particle characteristics were derived from a *single* and *nonintrusive* measurement technique. Flame temperature profiles were measured in the presence of particles by *in situ* Fourier transform infrared spectroscopy and thermophoretic sampling was used to visualize particle growth with height above the burner as well as in the radial direction. © 2005 American Institute of Physics. [DOI: 10.1063/1.1855391]

## I. INTRODUCTION

Aerosol combustion processes are commonly used to produce nanostructured metal-oxide and carbon powders for a wide range of industrial and research uses. The particle size is controlled mainly through the flame temperature, residence time of nanoparticles in high temperature regions of the flame, and through reactant mixing.<sup>1-3</sup> Particle sizes ranging from about 1 nm to 1  $\mu\text{m}$  can be produced with this continuous process. Depending on reactor residence time and material property, single particles or aggregates of (primary) particles are formed. Thereby, aggregates (sometimes called hard agglomerates) are primary particles connected by chemical bonds, while (soft) agglomerates are connected by physical (van der Waals, electrical, etc.) bonds following Friedlander.<sup>4</sup> Aggregates display mass-fractal scaling at size scales between the primary-particle diameter and the aggregate diameter.<sup>5</sup> Typically the mass-fractal dimension of collected powders is observed to be close to 2. In addition to primary and secondary structures in these powders, the aggregates are believed to cluster to form microscale soft agglomerates.

Recently, a detailed quantitative comparison between the average primary-particle diameters obtained from nitrogen adsorption (BET) and from ultra-small-angle x-ray scattering (USAXS) analysis was carried out for 75 different silica powders.<sup>6,7</sup> Excellent agreement was found between these two techniques when the USAXS diameter was derived from the same moment (volume to surface)<sup>7</sup> as the one measured by BET. Furthermore, aggregated and nonaggregated silica could be distinguished and the effect of process parameters on the final product powder characteristics such as primary and aggregate diameter and mass-fractal dimension was studied.<sup>6,7</sup> In the present study, we demonstrate that this technique can be applied to a dynamic system such as a flame aerosol reactor to study the growth dynamics of silica nanoparticles. Information about primary-particle and aggregate growth with distance from the burner or as function of particle residence time can be obtained nonintrusively, similar to the real-time monitoring of growing Pd nanoparticles on MgO(001) films or Co on Au(111) films studied by grazing incidence SAXS (Ref. 8) or probing the primary-particle growth dynamics in a diffusion flame.<sup>9</sup>

*In situ* techniques are appealing for gaining insight to the dynamics of particle growth. Dynamic light scattering (DLS), for instance, can measure nanoscale particle characteristics through the observation of particle motion. However, the temperature dependence of particle diffusivity and the inability of DLS to resolve aggregate substructure have

<sup>a)</sup>Present address: Clariant International Ltd., Masterbatches Division, CH-4132 Muttenz, Switzerland.

<sup>b)</sup>On sabbatical leave from the Department of Chemical and Materials Engineering, University of Cincinnati.

<sup>c)</sup>Author to whom correspondence should be addressed; electronic mail: beaucag@uc.edu

TABLE I. Gas flow rates, production rate, maximum flame temperature, and certain product powder characteristics for the two investigated silica nanoparticle producing premixed flames. Furthermore, the gas flow rates for the nonparticle producing background flames are given. Flow rates are given at standard temperature and pressure STP.

Flame	CH <sub>4</sub> L/min.	O <sub>2</sub> L/min.	N <sub>2</sub> L/min.	N <sub>2</sub> carrier for HMDSO L/min.	Total flow (STP) L/min.	Production rate g/h	Maximum temperature K	Filter powder			
								USAXS (BET) nm	PDI	$d_r$	$z$
Cold flame	0.4	1.4	5	1	7.8	14	2340	10.7 (10.8)	11.6	1.97	69
Background cold flame	0.4	1.4	3	1	5.8	0					
Hot flame	0.8	4.3	8.9	3	17	38	2480	26.2 (23.0)	6.5	1.96	22
Background hot flame	0.8	4.3	2.6	3	10.7	0					

limited application of DLS to flame reactors.<sup>10–13</sup> Static light scattering (SLS) is limited by the complexity of Mie theory for particles other than monodisperse, spherical structures, and approximations involved in the use of the Rayleigh–Gans theory for metal-oxide particles with large refractive indices. Additionally, the relatively large wavelength of light leads to size limitations in static measurements, nonetheless light scattering is ideal for direct measurement of aggregate size and mass-fractal dimension of larger aggregates.<sup>14–21</sup> Further, distinguishing weak scattered light from the flames high optical emissions is a major experimental hurdle for SLS. In most static light scattering techniques the primary-particle size or number of primary particles per aggregate has to be known *a priori* and is often determined with intrusive thermophoretic sampling (TS-TEM).<sup>17,19–22</sup> For ceramic oxides, Hurd and Flower,<sup>14,23</sup> for example, applied static and dynamic (using spectral broadening) light scattering to obtain the aggregate size and mass-fractal dimension especially for large aggregates.

X-ray scattering and especially ultra-small-angle x-ray scattering can overcome limitations inherent to classic light scattering techniques. USAXS is truly a nanoscale to microscale technique since its wavelength is four orders smaller than that of visible light. The minimum size for USAXS (described by the correlation distance  $\lambda/2$ , where  $\lambda$  is the wavelength) is on the order of 0.05 nm depending on the wavelength used. The difference in the effective refractive index is so small in USAXS that the Rayleigh–Gans approximation (no internal reflections, no internal particle refraction, particles act like point sources of reradiated waves) is wholly appropriate making generalized scattering laws such as the Guinier function and Porod’s law completely applicable.<sup>24</sup> USAXS measurements are not affected by flame emission, since the emitted spectrum does not reach x-ray wavelengths.

*In situ* measurements using USAXS are typically limited by the relatively low flux of laboratory x-ray sources compared to laser sources. For example, a 20 mW HeNe laser produces roughly 1000 times the number of photons per area as a laboratory tube x-ray source.<sup>25</sup> Laboratory x-ray sources are also uncollimated and have a short coherence length. Through the use of third generation synchrotron sources [European Synchrotron Radiation Facility, Grenoble, France, and Advanced Photon Source (APS) at Argonne National Laboratories, Chicago, USA] photon flux, coherence and collimation can be increased to levels comparable to that of

laser light sources enabling *in situ* flame studies.<sup>9</sup>

In the present experiments, a Bonse–Hart (BH) USAXS camera developed by the UNICAT team at the APS, Argonne National Laboratories<sup>26</sup> is used that can probe three to four orders of magnitude in size. Sizes up to 1  $\mu\text{m}$  can be routinely measured. For nanoparticles with primary sizes of 10 nm and aggregate sizes on the order of 100 nm the USAXS instrument is an ideal tool for their structural characterization. Due to the high flux available at the APS we were able to make reproducible measurements on nanoparticulate aerosols using concentrations typically employed in laboratory-scale flame aerosol reactors in a relatively short period of time. Our studies involved relatively well understood premixed flames using hexamethyldisiloxane (HMDSO) as a silica precursor operated to produce aggregated and almost nonaggregated silica particles. Specifically the primary-particle diameter, mass-fractal dimension, geometric standard deviation, silica volume fraction, number concentration, radius of gyration of the aggregate, and number of primary particles per aggregate can be simultaneously measured in a single experiment.

## II. EXPERIMENT

Two silica nanoparticle-producing flames were studied here. They were established with a honeycomb stabilized premixed burner (quartz glass, 25 mm inner diameter<sup>27</sup>). HMDSO (Fluka, 99%) was saturated in a thermostated bubbling flask and was then mixed with oxygen, methane, and more nitrogen (all 99.99% Praxair) before entering the burner. The flow rates were controlled with mass flow controllers (MKS Instruments) and are summarized in Table I. For USAXS background measurements, in the absence of particles, a premixed methane/oxygen flame with less nitrogen (Table I) was used to achieve similar flame shapes (flat flames) as in the particle-laden flames. A nitrogen sheath stream, which flowed through the outer quartz gap further stabilized the flame. The burner was attached to a computer controlled vertical/horizontal translation stage (Accudex, Aerotech Inc., Pittsburgh) with a precision of  $\pm 0.05$  mm for axial and lateral measurements.

Product powder was collected on glass fiber filters (Whatman GF/A) and its BET specific surface area (SSA) was determined by nitrogen adsorption (Tristar, Micromeritics Instruments Corp.). The average primary-particle diameter was calculated using  $d_{\text{BET}} = 6/(\rho_{\text{SiO}_2} \times \text{SSA})$ , with  $\rho_{\text{SiO}_2}$

$=2.2 \text{ g/cm}^3$ . The flame temperature was measured by emission/transmission spectroscopy<sup>27</sup> using an FTIR spectrometer (Bomem Inc., MB155S) operating in the range of  $6500\text{--}500 \text{ cm}^{-1}$  ( $1.5\text{--}20 \text{ }\mu\text{m}$ ) with  $2 \text{ cm}^{-1}$  resolution. Thermophoretic particle sampling (TS-TEM) (Ref. 28) is described in previous publications.<sup>29,30</sup>

As noted above, the USAXS measurements were conducted at the APS at Argonne National Laboratories, using the USAXS facility at UNICAT 33ID beam line.<sup>26</sup> Each scan (measuring intensity versus divergence angle) required  $\approx 20$  min per position in the flame since the BH camera requires a step scan through scattering angle. The flame was monitored via a TV camera during the measurements. The x-ray beam had a footprint of 2 mm by 0.4 mm and was oriented horizontally, parallel to the burner head, while the BH rocking curve was measured normal to the burner head.

The USAXS data was corrected for transmission and background using a particle-free premixed flame, as noted above, Table I. The corrected USAXS data were desmeared using the Lake method<sup>31</sup> and analyzed using the unified function for mass-fractal aggregates<sup>7,32–35</sup> both with software provided by UNICAT and available on-line at [www.uni.aps.anl.gov](http://www.uni.aps.anl.gov). USAXS data is easily converted to absolute intensity since the flux of the incident beam is measured during each USAXS scan. Each USAXS run is then a primary absolute intensity measurement (based on an estimated flame thickness).

### III. THEORY

The scattered intensity is measured as function of the momentum transfer or scattering vector  $q$  defined as  $q=4\pi \times \sin(\Theta/2)/\lambda$ , where  $\lambda$  is the wavelength of the incident photons and  $\Theta$  is the scattering angle. For large  $q$ , thus, small sizes ( $0.02 \text{ }\text{\AA}^{-1} < q < 0.07 \text{ }\text{\AA}^{-1}$ ), the scattered intensity  $I(q)$  decays with a power law<sup>24,25,36</sup> following:

$$I(q) = B_{\text{Porod}} q^{-4} \quad (1)$$

where

$$B_{\text{Porod}} = 2\pi r_e^2 N(\Delta\rho)^2 S,$$

reflecting Rayleigh–Gans scattering from a smooth and sharp interface (Fig. 1).  $B_{\text{Porod}}$  is the Porod prefactor,  $r_e^2$  the electron cross section,  $N$  the particle number density,  $\Delta\rho$  the electron density versus air, and  $S$  the particle surface area. The scattering parameters used in this section are defined and summarized in Table II together with the corresponding units. The scattering regime described in Eq. (1) is referred to as the Porod regime and is preceded at lower  $q$ , by two knee-like decays (Guinier regimes) in the logarithm of intensity versus  $q$ , that reflect the primary-particle size  $0.01\text{--}0.04 \text{ }\text{\AA}^{-1}$  (Fig. 1), and aggregate size  $0.001\text{--}0.006 \text{ }\text{\AA}^{-1}$  (Fig. 1), respectively. The scattering for these regimes follows Guinier's law,<sup>24,25,36</sup>

$$I(q) = G \exp\left(-\frac{q^2 R_g^2}{3}\right) \quad (2)$$

where

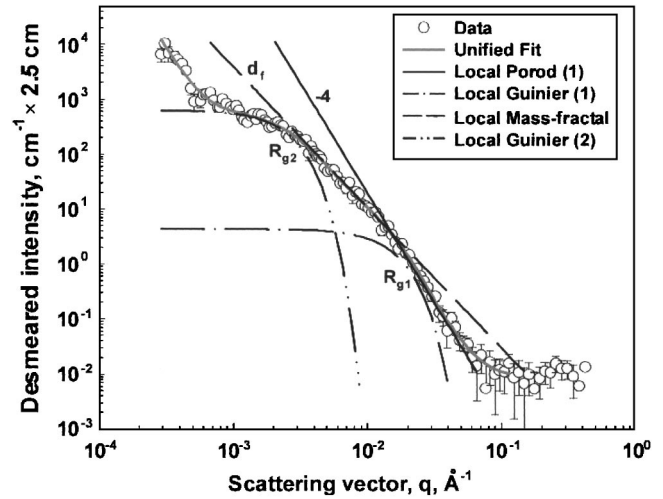


FIG. 1. *In situ* measured desmeared scattered intensity (circles) as a function of the scattering vector  $q$  for the hot flame at 40 mm HAB. The scattering data are well described by the unified fit (solid gray line). Furthermore, component curves of the global unified fit are shown such as the Porod regime for primary particles (solid black line), the Guinier regime for primary particles (dash-dotted line), and aggregates (dash-double dotted line). The appearance of a weak power-law regime ( $0.004 \text{ }\text{\AA}^{-1} < q < 0.02 \text{ }\text{\AA}^{-1}$ ) indicates that these particles are mass fractal. Intensity has not been normalized for flame thickness so the observed value of absolute intensity should be divided by 2.5 cm as indicated.

$$G = r_e^2 N(\Delta\rho)^2 V^2.$$

Here,  $G$  is the Guinier prefactor,  $R_g$  the radius of gyration, and  $V$  the particle or aggregate volume. Between the Guinier regime associated with primary-particle size and that associ-

TABLE II. Overview of the scattering and calculation parameters from the USAXS evaluation along with their corresponding units.

Scattering parameter	Units	Referring to	
$I(q)$	Scattered intensity	$\text{cm}^{-1}$	...
$q$	Scattering vector	$\text{\AA}^{-1}$	...
$G_1$	Guinier prefactor	$\text{cm}^{-1}$	Primary particles
$G_2$	Guinier prefactor	$\text{cm}^{-1}$	Aggregates
$R_{g1}$	Radius of gyration	$\text{\AA}$	Primary particles
$R_{g2}$	Radius of gyration	$\text{\AA}$	Aggregates
$B_{\text{Porod}}$	Porod prefactor	$\text{cm}^{-1} \text{\AA}^{-4}$	Primary particles
$B_f$	Power-law prefactor	$\text{cm}^{-1} \text{\AA}^{-d_f}$	Aggregates
$d_f$	Mass-fractal dimension	-	Aggregates
$Q$	Porod invariant	$\text{cm}^{-1} \text{\AA}^{-3}$	Primary particles
Calculation parameter	Units	Value	
$r_e^2$	Electron cross section	$\text{cm}^2$	$7.94 \times 10^{-26}$
$N$	Particle number density	$\text{cm}^{-3}$	Eq. (8)
$\Delta\rho$	Electron density vs air	$\text{cm}^{-3}$	Eq. (9)
$S$	Particle surface area	$\text{m}^2$	Primary particles
$V$	Particle volume	$\text{cm}^3$	Primary particles
$-P$	Power-law slope	...	var.
$N_c$	Number of electrons ( $\text{SiO}_2$ )	#	30
$M$	Molecular weight ( $\text{SiO}_2$ )	$\text{g/mol}$	60.1
$\rho$	Density ( $\text{SiO}_2$ )	$\text{g cm}^{-3}$	2.2
$N_A$	Avogadro number	#	$6.022 \times 10^{23}$
$\phi_v$	Silica volume fraction	...	Eq. (10)
$z$	No. of prim. particles per aggregate	#	Eq. (11)

ated with aggregate size, there is a shallow power-law decay reflecting the mass-fractal structure of the ramified aggregates. In this regime the scattering follows the power-law decay,

$$I(q) = B_f q^{-d_f}, \quad (3)$$

where  $d_f$  is the mass-fractal dimension of the aggregate and the constant  $B_f$  is defined by Beaucage.<sup>33–35</sup>

Since these four scattering functions significantly overlap during the scattering of aggregates, that themselves consist of primary particles, it is generally more useful to use global scattering functions to fit the entire scattering curve.<sup>7,32–35</sup> This global unified function is closely aligned to the local scattering laws (Porod's and Guinier's law) described above using a spherical, primary-particle model and mass-fractal aggregates where appropriate.<sup>35</sup>

In addition,  $B_{\text{Porod}}$  normalized by the integral of the part of the scattering curve associated with the primary particles  $Q$  (subscript 1) reflects the same moment of volume  $V$  to surface  $S$  as the particle size calculated from gas adsorption measurements using BET analysis and assuming spherical particles  $d_{V/S} = 6 V/S$  as demonstrated recently for various nanoparticles.<sup>6,7</sup> This is a useful value since gas adsorption is a common analysis method for powder with large specific surface areas, while a primary-particle size obtained from  $R_{g1}$ , as often done in literature, is a ratio of high order moments and heavily weights large particles.<sup>7</sup> The Porod invariant  $Q$  is defined by<sup>7,36</sup>

$$Q = \int_0^\infty q^2 I(q) dq = 2\pi^2 r_e^2 N(\Delta\rho)^2 V \quad (4)$$

and  $d_{V/S}$  is given by

$$d_{V/S} = 6 \frac{Q}{\pi B_{\text{Porod}}} = 6 \frac{V}{S}. \quad (5)$$

A lack of an intersection between the Guinier, Eq. (2) (dashed-dotted line in Fig. 1), and Porod, Eq. (1) regimes (black line in Fig. 1), as shown in Fig. 1 at  $q=0.025 \text{ \AA}^{-1}$  indicates that the primary particles are polydisperse.<sup>7</sup> A measure of primary-particle polydispersity is the ratio of the interpolated Porod intensity at  $R_g$ ,  $B_1 R_{g,1}^4$ , Eq. (1), to the Guinier prefactor for the primary particles,  $G_1$ , Eq. (2). This unitless polydispersity index (PDI) can be directly obtained from the scattering experiment without assumptions concerning particle shape or the functionality of the size distribution:

$$\text{PDI} = \frac{B R_g^4}{1.62 G}. \quad (6)$$

For monodisperse spheres, PDI is 1, while a PDI of 4.93 or 5.56 is obtained for the self-preserving limit<sup>7</sup> in the continuum or free molecular transport regimes, respectively, of self-preserving distributions consisting of spherical particles.<sup>37</sup> A high value of PDI could also arise from asymmetry of particle shape or potentially from contrast gradients in the particles but TEM revealed that neither of these are important for the silica particles studied in this paper. With the assumption of a log-normal particle size distribution of spherical primary particles often found in single-source

aerosols,<sup>38</sup> the geometric standard deviation  $\sigma_g$  can be expressed in terms of the observed polydispersity index as<sup>7</sup>

$$\sigma_g = \exp(\sigma) = \exp\left(\sqrt{\frac{\ln(\text{PDI})}{12}}\right). \quad (7)$$

Here,  $\sigma$  is the corresponding standard deviation of the logarithm of particle size. Both  $\sigma_g$  and PDI are reported since the primary-particle size distributions may not be perfectly log-normal and because PDI is directly related to the observed data and does not rely on assumptions.

The number density of primary particles in the aerosol stream  $N$  can be calculated from the Porod invariant  $Q$  and the Guinier prefactor  $G_1$  using Eqs. (2) and (4),

$$N = \frac{Q^2}{4\{r_e^2(\Delta\rho)^2\}\pi^4 G}. \quad (8)$$

The absolute contrast factor  $\{r_e^2(\Delta\rho)^2\}$  is calculated from

$$r_e^2(\Delta\rho)^2 = r_e^2 \left(\frac{N_A \rho N_e}{M}\right)^2 = 3.473 \times 10^{22} \text{ cm}^{-4}, \quad (9)$$

for silica in vacuum, where  $N_A$  is Avogadro's number,  $N_e$  the number of electrons in an  $\text{SiO}_2$  molecule, and  $M$  the corresponding molecular weight. Values for these and other constants used in this article are listed in Table II. Under the assumption of uniform density  $\rho$  of  $2.2 \text{ g/cm}^3$  for the primary particles, the absolute intensity can yield directly the number density of primary particles.

The volume fraction of silica in the irradiated volume of the flame  $\phi_{V,\text{silica}}$  can be calculated from the Porod invariant  $Q$ , Eq. (4), and the contrast for silica, Eq. (9),

$$\phi_V = \frac{Q}{2\pi^2 r_e^2(\Delta\rho)^2}, \quad (10)$$

where  $\phi_V$  gives an indication of the total volume fraction of silica species in the aerosol.

Using Eq. (2) for the aggregates and primary particles, it is possible to directly measure the weight average number of primary particles in an aggregate  $z$ . This value is often of more use in characterizing aggregate structure than the radius of gyration  $R_{g2}$  since the radius of gyration reflects a high order moment of the size distribution, so the largest aggregates dominate the  $R_g$  value.<sup>7</sup> Writing Eq. (2) for primary particles and aggregates,<sup>34</sup>

$$z = \frac{G_2}{G_1} = \frac{N_2 n_{e,2}^2}{N_1 n_{e,1}^2} = \frac{(N_1/z)(n_{e,1}z)^2}{N_1 n_{e,1}^2}, \quad (11)$$

where "1" refers to the primary particles and "2" refers to the aggregates and  $n_e = (\Delta\rho V)$ . The degree of aggregation  $z$  is independent of any structural model and only relies on the assumption that level 2 is composed of level 1 structures. That is, it holds true for any mass-fractal dimension, topology, or connectivity of structure (branch content). Further, this measure of  $z$  does not rely on absolute intensity since it is internally normalized.

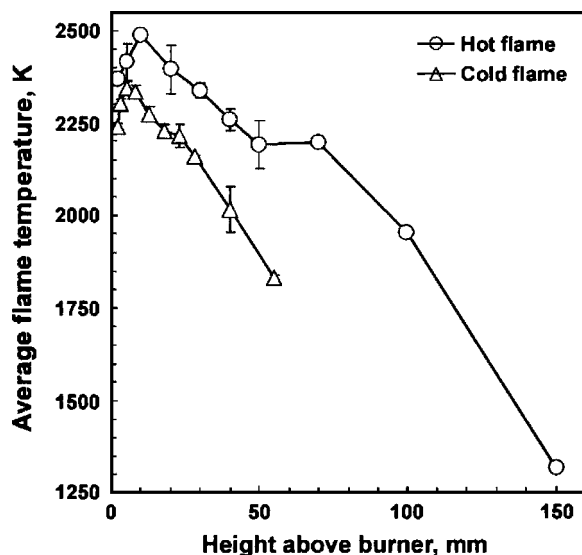


FIG. 2. Axial flame temperature profiles of the cold (triangles) and hot (circles) flame along the centerline measured by *in situ* FTIR emission/transmission spectroscopy.

#### IV. RESULTS AND DISCUSSION

Two premixed flames were studied, a flame with a relatively colder temperature with low precursor concentration, referred as cold flame (Table I), that produces aggregated silica at 14 g/h, and a flame with relatively higher flow rates that is hotter and that produces relatively large, mostly non-aggregated silica particles far from the burner, referred to as hot flame (Table I), at a rate of 38 g/h silica.

Figure 1 shows typical scattering data obtained from *in situ* USAXS measurements on silica flames for the hot flame at 40 mm height above the burner (HAB). At highest  $q$ , a flat background is evident which may be associated with excess  $\text{CO}_2$  present in the silica flames compared with the background flames of Table I. The scattering curve displays mass-fractal structures as described above. Scattering data (circles) were fit using the global unified function (gray solid line).<sup>7,32–35</sup> The dashed-dotted and dashed-double dotted lines show the local Guinier calculation [Eq. (2)] for primary particles and aggregates, while the black solid and the dashed lines shows the local Porod calculation [Eq. (1)] and the local mass-fractal calculation [Eq. (3)], respectively, using the values obtained from the global unified fit (gray solid line). For a more detailed description of the evaluation see Beaucage,<sup>7,32–34</sup> Hyeon-Lee *et al.*,<sup>35</sup> or Kammler *et al.*<sup>6</sup> Even though the scattering curves were obtained *in situ*, with silica volume fractions of  $\sim 10^{-6}$ , particle scattering is sufficient for analysis. In the cold flame, however, the particle scattering above 40 mm HAB was too low for reliable data evaluation and was not considered in the following evaluation. At the lowest  $q$  in Fig. 1 ( $< 7 \times 10^{-4} \text{ \AA}^{-1}$ ) a Porod tail, Eq. (1), is seen which might be associated with agglomerates or clusters of aggregates.

Figure 2 shows axial flame temperature profiles of the cold (triangles) and hot (circles) flame, which were measured in the presence of particles by *in situ* Fourier transform infrared (FTIR) emission/transmission spectroscopy.<sup>27</sup> The maximum axial temperature was 2350 K at 5 mm HAB for

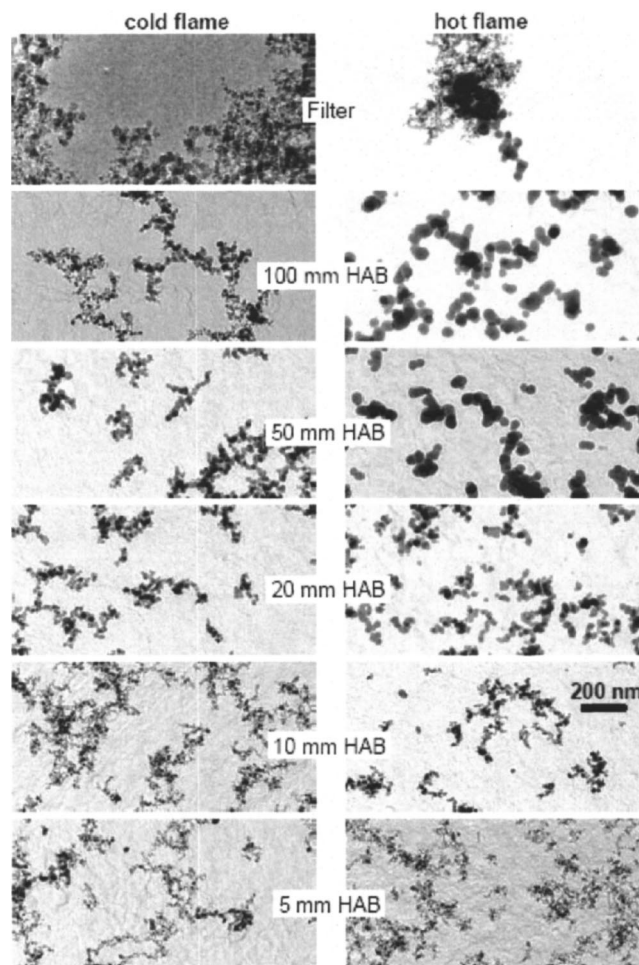


FIG. 3. Thermophoretically sampled TEM pictures at different heights above the burner for the cold flame (left-hand side) and the hot flame (right-hand side) along with TEM pictures of the respective filter powders.

the cold flame and 2490 K for the hot flame (at 10 mm HAB). Both temperature profiles decrease almost linearly further downstream. The  $\approx 100$  K higher maximum temperature for the hot flame is predicted by comparing the adiabatic flame temperatures of the two flames. The temperature was 1830 K at 55 mm HAB, for instance, for the cold flame, while for the hot flame, at 100 mm HAB a value of 1960 K was measured.

Figure 3 shows snapshots of particle growth obtained by thermophoretic sampling (TS-TEM) at different heights above the burner. Since the hot flame has a higher maximum flame temperature, a prolonged high temperature zone (Fig. 2), and an initial silica concentration of 1.25 times higher than the cold flame, silica particles grow longer, resulting in larger particles, as shown in the TEM pictures (Fig. 3). The average primary-particle size appears to be almost constant at positions  $\geq 20$  mm HAB for the cold flame. For the hot flame the particle size further increases at higher positions because of the extended high temperature region (Fig. 2) which results in almost spherical, nonaggregated (or weakly aggregated) particles  $\geq 50$  mm HAB. For the cold flame, however, aggregated particles are observed throughout the flame. At the filter, mixtures of aggregates with smaller and larger primary-particle sizes are detected as will be discussed

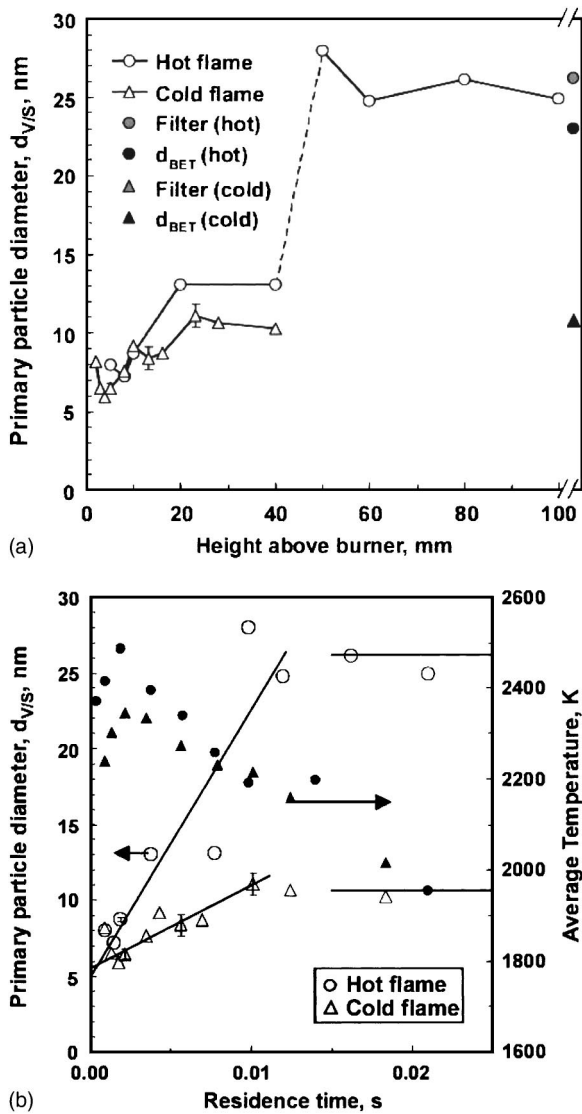


FIG. 4. (a) Evolution of the primary particle size obtained from the *in situ* measured USAXS volume to surface ratio  $d_{V/S}$  with height above the burner measured along the centerline for the cold flame (triangles) and the hot flame (circles). Filter powder values are also shown. (b) shows the same data (open symbols, left axis) but with respect to residence time, assuming a plug flow reactor model and ideal gases along with the corresponding temperature profile (see Ref. 9) (filled symbols, right axis). The primary particle growth rate in the hot flame is about three times that of the cold flame.

in detail below, however, the primary-particle sizes within the aggregates are relatively uniform (Fig. 3).

### A. Primary-particle growth dynamics

Figure 4 shows the average primary-particle diameter  $d_{V/S}$  along the burner axis obtained from the USAXS volume to surface ratio, Eq. (5), as a function of height above the burner [Fig. 4(a)] and the corresponding residence time [Fig. 4(b)] for the two flames, which was calculated assuming a plug flow reactor model and ideal gases along with the corresponding temperature profile.<sup>9</sup> Very close to the burner the average primary-particle diameter decreases for the cold flame from 8 nm (at 2 mm HAB) to 6 nm (at 4 mm HAB) and for the hot flame from 8 nm (5 mm HAB) to 7 nm (8 mm HAB). Then the primary-particle size increases

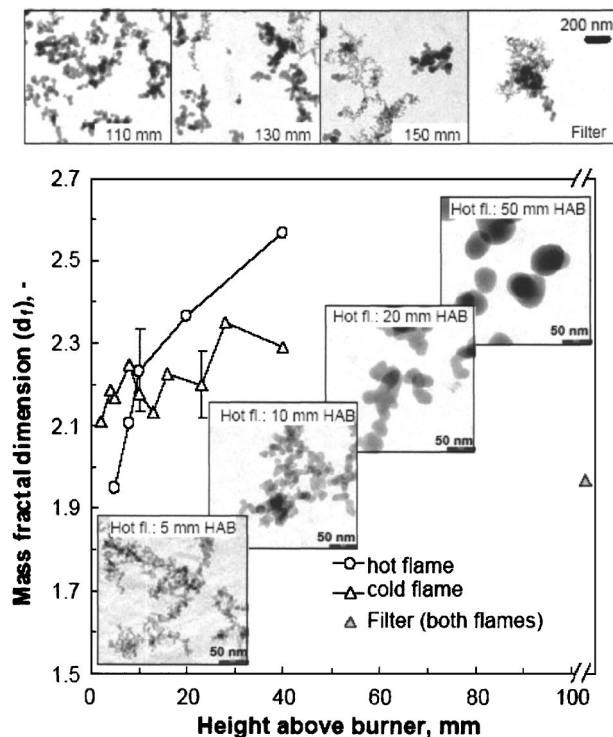


FIG. 5. Evolution of the mass-fractal dimension  $d_f$  with height above the burner obtained from *in situ* USAXS along the centerline for the cold flame (triangles) and the hot flame (circles). Thermophoretically sampled TEM pictures from the hot flame are inserted for various heights above the burner to visualize also the aggregate structure. Filter powder values are also shown.

monotonically up to 11 nm at 23 mm HAB for the cold flame and up to 25 nm at 60 mm HAB for the hot flame. At these heights the average primary-particle diameter remains rather constant until collection on the filter [Fig. 4(a), filled circle], in agreement with intrusive TS-TEM studies in  $\text{TiO}_2$  laden premixed flames by Arabi-Katbi *et al.*<sup>39</sup> or Kammler *et al.*<sup>30</sup> The dashed line [Fig. 4(a)] indicates the transition between aggregated (<50 mm HAB) and nonaggregated particles (50–100 mm HAB) as will be shown in detail in Fig. 5. The average flame temperature at these points (23 mm HAB for the cold flame and at 60 mm HAB for the hot flame) is rather similar, namely, 2200 K. The residence time in the region of rapid particle growth (>2200 K) is very similar for both flames [Fig. 4(b)]. However, the initial particle growth rate [indicated by the solid lines in Fig. 4(b)] is about three times faster in the hot flame since it is significantly hotter (Fig. 2) and has an initial particle volume fraction 1.2 times higher with respect to the cold flame. Both the higher concentration and temperature lead to the formation of larger primary particles in the hot compared to the cold flame. The significant slow down in primary-particle growth rate at 2200 K appears for both flames at similar total residence time [Fig. 4(b)] but still above the melting point of nanoscale silica (1983 K) (Ref. 40).

The initial decrease in particle size (HAB < 10 mm) might be supported by a few, scattered, large particles detected by TS-TEM at low heights (5 mm HAB) for the cold flame (Fig. 3) that were not detected further downstream. Similarly, quite irregularly shaped particles were detected in

hot wall reactors where, at low temperatures, the chemical reaction was not fully completed.<sup>41</sup> The reported particles, in that study,<sup>41</sup> were proposed to be partially oxidized  $\text{SiO}_x\text{C}_y\text{H}_z$ .

Furthermore, the decrease in average primary-particle size low in the flames coincides with a rapid increase in particle number concentration at 4 and 8 mm HAB for the cold and hot flame, respectively, as will be shown later. Therefore, the initial decrease in mean particle size is associated with the nucleation behavior. At low volume fraction and low temperature (i.e., low supersaturation), the formation of larger particles is favored (Gibbs–Thomson equation), while at high supersaturation (high volume fraction and high temperature) smaller particles are formed which outnumber the fewer larger ones. Therefore, the average primary-particle diameter can decrease (Fig. 4). Using SLS and TS-TEM, a similar decrease in primary-particle diameter close to the burner was also observed by Hurd and Flower<sup>14</sup> for silica and Koylu *et al.*<sup>20</sup> for soot.

The silica concentration was too low for reliable *in situ* measurements above about 40 mm for the cold flame, while the 1.2 times higher initial silica volume fraction and 2.2 times higher total gas flow rates enabled measurements further downstream for the hot flame.

The hot flame differs markedly in aggregation behavior from the cold flame as shown in axial data, Fig. 5. Mass-fractal aggregates with  $d_f$  of 2.1 are formed close to the burner in the cold flame. Later, they become slightly more compact which is corroborated by  $d_f$  increasing up to 2.3 (Fig. 4). However, for the hot flame,  $d_f$  increases steadily from 2 at 5 mm HAB to 2.6 at 40 mm HAB. The increase in branch content can also be qualitatively seen in the corresponding TEM inserts to Fig. 5, though it is partially obscured by primary-particle growth. At  $\text{HAB} > 40$  mm, USAXS measurements indicate that the fractal structure vanishes as the scattering curve can be described well without considering an intermediate fractal power-law regime<sup>6,7,35,42</sup> indicating nonaggregated particles. The TS-TEM at 50 mm HAB (TEM insert) supports this result showing almost completely coalesced single, doublet, or triplet particles, thus nonaggregated single particles. Similar particle morphologies are observed both by SAXS and TS-TEM for higher locations [at 70, 90, and 100 mm HAB (all not shown)].

The evolution of  $d_f$  with HAB agrees with work of Hurd and Flower<sup>14</sup> ( $d_f=1.5$ , for measurements close to the burner in silica premixed flames, using static light scattering), Xing, Koylu, and Rosner<sup>19</sup> ( $d_f$  of  $\text{Al}_2\text{O}_3$  measured by laser light scattering which increases from 1.6 to 1.8 with increasing residence time in the flame in a counterflow diffusion flame), and the work of Choi *et al.*<sup>22</sup> ( $d_f=2.4$ , for measurements higher up in a silica flame, using LS/TS-TEM). However, it should be pointed out that even though Xing, Koylu, and Rosner<sup>19</sup> or Choi *et al.*<sup>22</sup> determined local  $d_f$  from LS in alumina and silica particle-laden flames, respectively, the knowledge of the average primary-particle diameter was required which both groups determined by independent intrusive TS-TEM measurements.

Product powders collected on the filter made in the hot and the cold flame show a  $d_f$  of about 2 (Table II), which

disagrees with the highest axial measurements for both flames. This may be related to the formation of larger aggregates with smaller primary-particle sizes in the colder parts of the flame especially at the flame edges, which were clearly evident in off-center SAXS measurements (not presented) and which are visualized here by radial TS-TEM at 50 mm HAB in hot flame as shown in Fig. 6. The radial flame temperature profile of such particle-laden premixed flames is relatively homogeneous in the flame center ( $r=0-6$  mm), however, as a result of dilution with surrounding air and radiation losses the flame temperature decays close to the burner edge.<sup>27</sup> As the particle and aggregate growth strongly depend on temperature, in these colder regions highly aggregated particles consisting of small primary particles are formed as can be observed at  $r=15$  mm (beyond the burner edge, which is at  $r=12.5$  mm). At  $r=12$  and 9 mm, aggregates of intermediate primary-particle sizes are observed as well as a mixture of large aggregates from the flame edge and almost completely coalesced particles from the flame center (Fig. 6).

At  $\text{HAB} > 100$  mm, particle collisions do not result in complete coalescence and aggregation can be observed (TEM and filter powder data points on the right-hand side of Fig. 5) as was also observed in  $\text{TiO}_2$  premixed flames by Arabi-Katbi *et al.*<sup>39</sup> by TS-TEM. Furthermore, with increasing HAB, aggregates consisting of significantly smaller primary particles similar to those detected at the flame edges are observed together with the larger only slightly aggregated particles. This can be explained by the onset of mixing of different streamlines, thus the detected aggregates consisting of small primary particles were formed at the flame edges and move to the flame center by entrainment.

At the filter (Figs. 3 and 5) particles formed along all the different streamlines of the flame are collected, where different growth conditions may have lead to significantly different aggregation phenomena. A mixture of aggregates consist of an average  $d_f$  of about two results. This result may even explain the rather insensitive effect of process parameters on the product powder  $d_f$  as observed recently by Kammler *et al.*<sup>6</sup>

### **Evolution of the width of the primary-particle size distribution**

Using Eqs. (6) and (7), the width of the primary-particle size distribution (PPSD) can be directly derived from the scattering parameters in terms of the polydispersity index, PDI, or assuming spherical particles and a log-normal size distribution,<sup>38</sup> in terms of the geometric standard deviation,  $\sigma_g$ .<sup>7</sup> Figure 7 shows the evolution of the  $\sigma_g$  (left axis) and PDI (right axis) with height above burner for both flames. Very close to the burner, the PPSD appears to be wide, then becomes even narrower than the self-preserving size distribution in the free molecular regime for both flames. Upon ongoing particle formation the PPSD broadens especially for the cold flame. With increasing height, also the  $\sigma_g$  of the hot flame reaches the self-preserving limit of  $\sigma_g=1.45$  (PDI = 5.56) and becomes even slightly larger when only fully coalesced particles are observed ( $>40$  mm HAB). However,  $\sigma_g$  of the filter powder of the hot flame is very close to the

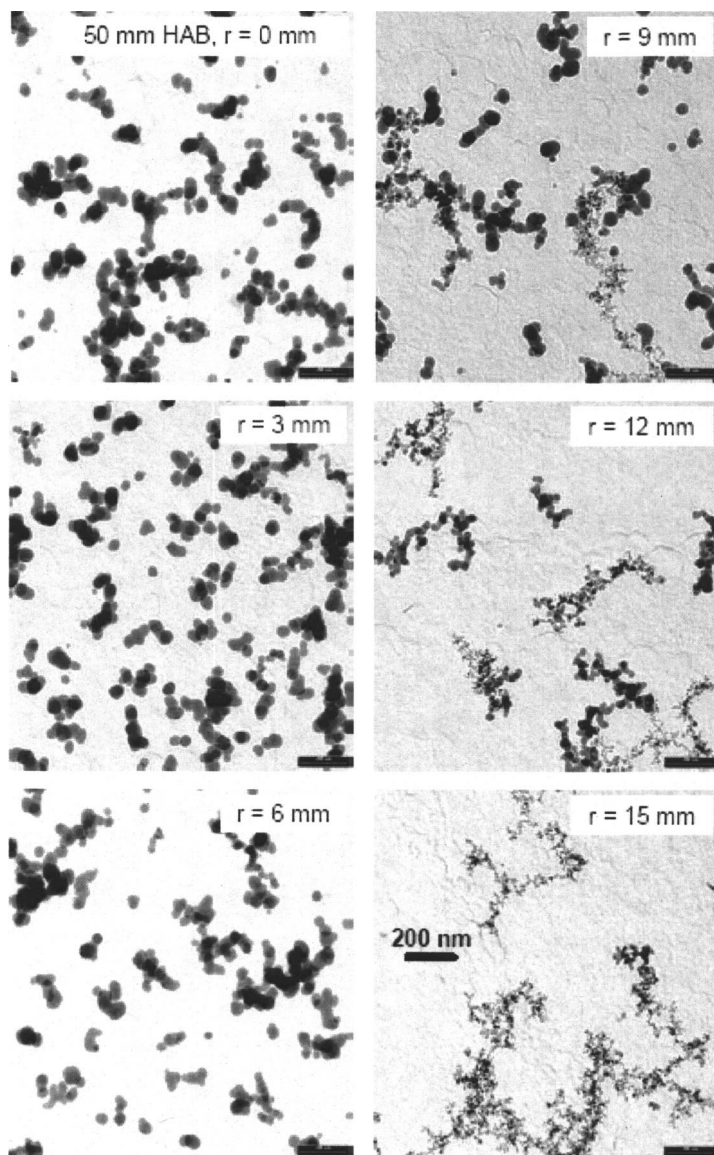


FIG. 6. Thermophoretically sampled TEM pictures sampled at various radial positions  $r$  at a constant height above the burner of 50 mm obtained in the hot flame. ( $r=0$  refers to the centerline, while the burner edge is at  $r=12.5$  mm.)

self-preserving limit, while it is around 1.55 for the cold flame. This is consistent with data from monitoring the particle growth of titania nanoparticles by TS-TEM,<sup>30</sup> where similar values for  $\sigma_g$ , also below the self-preserving limit, were measured close to the burner and larger values were obtained further downstream.

### B. Silica volume fraction and particle number density

Figure 8(a) shows the total silica volume fraction  $\phi_V$  as determined from Eq. (10) with height above the burner.  $\phi_V$  accounts for all silica species present in the flame. Particle nucleation occurs when  $\phi_V$  reaches a critical value for homogeneous nucleation or a parallel critical value for chemical nucleation.<sup>43</sup> When the critical value is reached three signatures of nucleation are observed; a burst in number density [Fig. 8(b)], a minimum in particle size [Fig. 4(a)], and a peak in  $\sigma_g$  or PDI (Fig. 7), the latter associated with rapid nucleation under variable flame conditions of  $T$  and  $\phi_V$ .<sup>8</sup>

Both flames show a rapid rise in  $\phi_V$  to a maximum value of  $1.7 \times 10^{-6}$  and  $2.1 \times 10^{-6}$  in the cold and hot flame, respectively, at 4 and 8 mm. Homogeneous nucleation is fol-

lowed by coagulation and growth of nanoscale primary particles (Fig. 4).<sup>29,44,45,43</sup>  $\phi_V$  is depleted further downstream due to diffusion by Brownian motion, mixing and dilution with ambient air (Fig. 8). The measured shape of the  $\phi_V$  profile as well as the range of the obtained values agrees with axial light scattering measurements of Sorensen *et al.*,<sup>46</sup> Chang and Biswas,<sup>16</sup> and Choi *et al.*<sup>22</sup> The ratio of maximum concentration of silica for the cold and hot flame in Fig. 8(a) is 1.23, which is almost identical to their initial silica concentration ratio of 1.25 that was calculated from the precursor vapor pressure and carrier gas flow rate.

Figure 8(b) shows the number density  $N$  of silica particles with height above the burner. Particle nucleation is reflected by a sharp increase in number density having a maximum at about 3 mm HAB for the cold flame and 8 mm HAB for the hot flame.  $N$  then decays rapidly for both flames, similar to the observation for silica volume fraction (Fig. 8). The initial decay in  $N$  may indicate particle coagulation.<sup>29</sup> Further downstream the number concentration decreases due to dilution with ambient air.

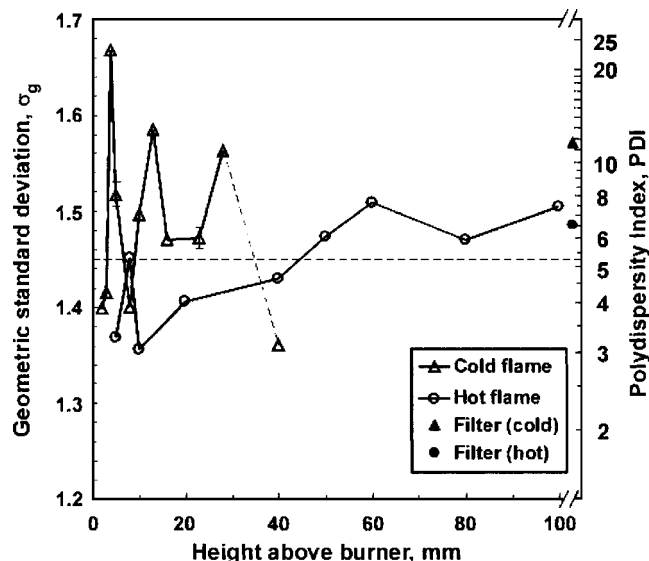
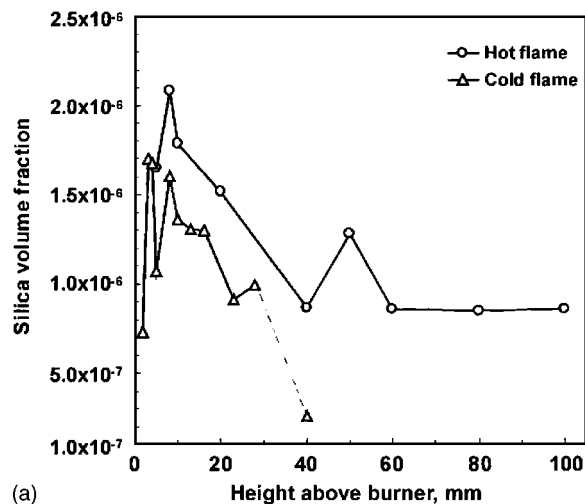


FIG. 7. Evolution of the geometric standard deviation,  $\sigma_g$  (left axis), and polydispersity index, PDI (right axis), with height above the burner obtained from *in situ* USAXS along the centerline for the cold flame (triangles) and the hotter flame (circles). The dashed line indicates the self-preserving limit for coagulation in the free molecular regime. Filter powder values are also shown. [Right axis is calculated using Eq. (7)].

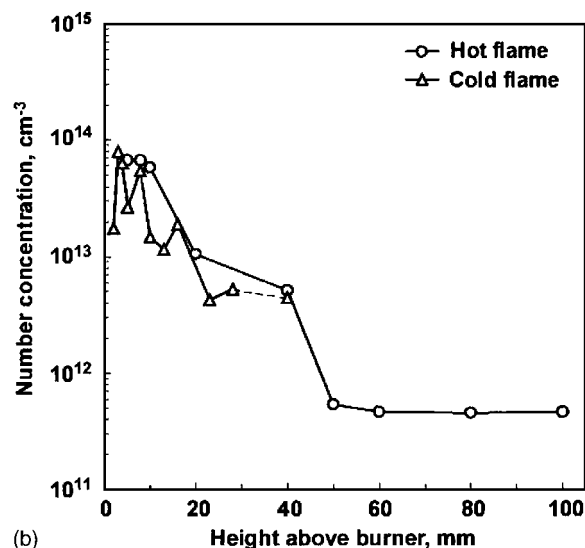
### C. Growth of aggregates

The evolution of the radius of gyration of the aggregate  $R_{g2}$  is presented in Fig. 9(a) with increasing HAB. Close to the burner,  $R_{g2}$  increases rapidly for the cold flame and reaches a maximum of about 135 nm at 3 mm HAB, where also the maximum number concentration and volume fraction were measured. Similarly, for the hot flame, large aggregates were measured close to the burner. After peaking,  $R_{g2}$  sharply decreases to about 75 nm for cold flame and 40 nm for the hot flame before increasing to almost constant values of 100 and 75 nm, respectively, up to about 40 mm HAB. This restructuring was also observed by di Stasio<sup>15</sup> for soot aggregate formation, and may be related to the rapid increase in flame temperature and ongoing particle growth by coagulation and sintering.<sup>19</sup> For the hot flame, nonaggregated particles are observed at HAB > 40 mm, while  $\phi_V$  was too low for reproducible measurements at similar positions for the cold flame as discussed above. The measured  $R_{g2}$ s are in qualitative agreement with the TS-TEM pictures (Fig. 3). An average equivalent end-to-end distance of these aggregates could be calculated by  $[(1+2/d_f)(2+2/d_f)]^{1/2}R_{g2}$ ,<sup>33</sup> where this prefactor ranges from 2.48 for  $d_f=1.95$  to 2.11 for  $d_f=3$ , which are the minimum and maximum values obtained in this study.

$R_{g2}$  reflects a high order moment of aggregate size, so is indicative of the largest aggregates.<sup>34</sup> Another important parameter in describing aggregates is the number of primary particles per aggregate,  $z$ , from Eq. (11) which is plotted in Fig. 9(b) as a function of HAB.  $z$  is the weight average so it should reflect more clearly the mean aggregate size.<sup>34</sup> The number of primary particles per aggregate is largely close to the burner where most of the particle formation occurs and decays, similar to the evolution of  $R_{g2}$ , with increasing HAB.  $z$  decreases when coalescence takes place at high tempera-



(a)



(b)

FIG. 8. (a) Evolution of the silica volume fraction (volume concentration) with height above the burner obtained from *in situ* USAXS along the centerline for the cold flame (triangles) and the hot flame (circles). (b) Evolution of the silica number concentration with height above the burner obtained from *in situ* USAXS along the centerline for the cold flame (triangles) and the hot flame (circles).

tures due to aggregate collapse.  $\phi_V$  was too low to perform measurements of  $R_{g2}$  in the colder flame regions (>100 mm HAB) where a secondary onset of aggregate formation along with significant mixing of the particles grown along different streamlines was observed (Fig. 5).

### V. CONCLUSIONS

USAXS was extended from measuring powder samples to an *in situ* technique that can follow the dynamics of ceramic nanoparticle growth in continuous flame reactors. We demonstrated here that it is possible to follow simultaneously the primary nanoparticle and aggregate growth in flames with a single *in situ* measurement. For a relatively well known system of two different premixed silica particle producing flames the USAXS measurement was shown to yield the evolution of primary-particle diameter, mass-fractal dimension, geometric standard deviation, silica volume fraction, number concentration, aggregate size, and number of

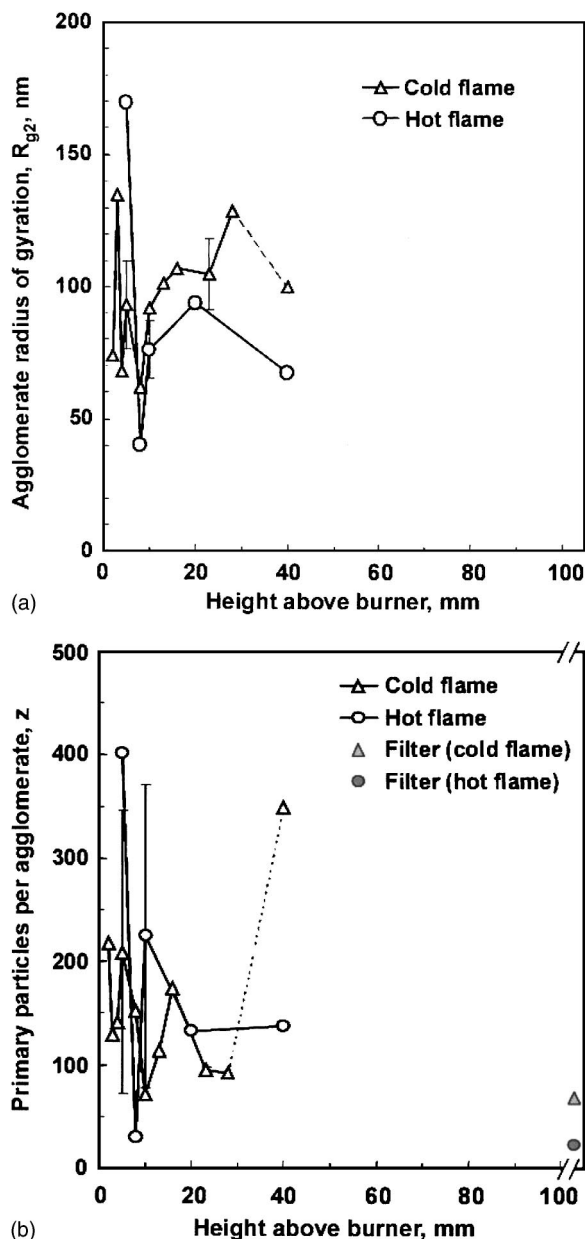


FIG. 9. (a) Evolution of the radius of gyration of the aggregate  $R_{g2}$  with height above the burner obtained from *in situ* USAXS along the centerline for the cold flame (triangles) and the hot flame (circles). (b) Evolution of number of primary particles per aggregate  $z$  with height above the burner obtained from *in situ* USAXS along the centerline for the cold flame (triangles) and the hot flame (circles). Filter powder values are also shown. For the hot flame, nonagglomerated particles are observed  $>50$  mm HAB, while for the cold flame the number concentration was too low for reproducible measurements  $>40$  mm HAB.

primary particles per aggregate. The nanoparticle growth dynamics were monitored with a single noninvasive measurement stepwise with height above the burner, which is a significant improvement compared to earlier *in situ* light scattering measurements, where always intrusive thermophoretic sampling for TEM had to be applied additionally for determining the average primary particle diameter and the number of primary-particles per aggregate. The *in situ* USAXS results largely agree with TS-TEM measurements at similar flame heights and with previously published static light scattering measurements.

Conventional SAXS pinhole measurements are also possible with the advantage of a much faster measurement time ( $<1$  s with a synchrotron source) but with a more limited  $q$  range ( $0.001$  to  $1 \text{ \AA}^{-1}$ ).<sup>8</sup> SAXS and USAXS can yield kinetic growth information for primary particles and mass-fractal aggregates in a single *in situ* measurement on an aerosol stream at low concentrations if sufficient x-ray flux is available.

## ACKNOWLEDGMENTS

The authors acknowledge the stimulating discussions with Professor S. E. Pratsinis. This work was supported by the U.S. National Science Foundation (Grant No. CTS-0070214), Swiss National Science Foundation (Grant No. 200021-101901/1), and the Swiss Commission for Technology and Innovation (Grant No. TopNano21-5487.1). Use of the UNICAT beam line was through the support of NIST's Ceramics Division and the UNICAT collaborators. The UNICAT beam line at the Advanced Photon Source (APS) is supported by the University of Illinois at Urbana-Champaign, Materials Research Laboratory [U.S. Department of Energy (DoE), the State of Illinois-IBHE-HECA, and the National Science Foundation], the Oak Ridge National Laboratory (U.S. DoE), the National Institute of Standards and Technology (U.S. Department of Commerce), and UOP LLC. Use of the Advanced Photon Source was supported by the U.S. Department of Energy, Basic Energy Sciences, Office of Science, under Contract no. W-31-109-Eng-38. G.B. acknowledges a sabbatical leave from the University of Cincinnati spent partially at ETH Zurich where this article was written.

<sup>1</sup>S. E. Pratsinis, *Prog. Energy Combust. Sci.* **24**, 197 (1998).

<sup>2</sup>S. Vemury and S. E. Pratsinis, *Appl. Phys. Lett.* **66**, 3275 (1995).

<sup>3</sup>L. Madler, W. J. Stark, and S. E. Pratsinis, *J. Appl. Phys.* **92**, 6537 (2002).

<sup>4</sup>S. K. Friedlander, *Smoke, Dust, and Haze: Fundamentals of Aerosol Dynamics* (Oxford University Press, New York, 2000).

<sup>5</sup>R. J. Samson, G. W. Mulholland, and J. W. Gentry, *Langmuir* **3**, 272 (1987).

<sup>6</sup>H. K. Kammler, G. Beaucage, R. Mueller, and S. E. Pratsinis, *Langmuir* **20**, 1915 (2004).

<sup>7</sup>G. Beaucage, H. K. Kammler, and S. E. Pratsinis, *J. Appl. Crystallogr.* **37**, 523 (2004).

<sup>8</sup>G. Renaud *et al.*, *Science* **300**, 1416 (2003).

<sup>9</sup>G. Beaucage, H. K. Kammler, R. Mueller, R. Strobel, N. Agashe, S. E. Pratsinis, and T. Narayanan, *Nat. Mater.* **3**, 370 (2004).

<sup>10</sup>G. B. King, C. M. Sorensen, T. W. Lester, and J. F. Merklin, *Phys. Rev. Lett.* **50**, 1125 (1983).

<sup>11</sup>T. W. Taylor and C. M. Sorensen, *Appl. Opt.* **25**, 2421 (1986).

<sup>12</sup>C. Oh and C. M. Sorensen, *J. Aerosol Sci.* **28**, 937 (1997).

<sup>13</sup>C. M. Sorensen, *Aerosol Sci. Technol.* **35**, 648 (2001).

<sup>14</sup>A. J. Hurd and W. L. Flower, *J. Colloid Interface Sci.* **122**, 178 (1988).

<sup>15</sup>S. di Stasio, *J. Aerosol Sci.* **32**, 509 (2001).

<sup>16</sup>H. Chang and P. Biswas, *J. Colloid Interface Sci.* **153**, 157 (1992).

<sup>17</sup>J. Cho and M. Choi, *J. Aerosol Sci.* **31**, 1077 (2000).

<sup>18</sup>M. R. Zachariah and H. G. Semerjian, *AIChE J.* **35**, 2003 (1989).

<sup>19</sup>Y. Xing, U. O. Koylu, and D. E. Rosner, *Appl. Opt.* **38**, 2686 (1999).

<sup>20</sup>U. O. Koylu, C. S. McEnally, D. E. Rosner, and L. D. Pfefferle, *Combust. Flame* **110**, 494 (1997).

<sup>21</sup>U. O. Koylu, Y. C. Xing, and D. E. Rosner, *Langmuir* **11**, 4848 (1995).

<sup>22</sup>M. Choi, J. Cho, J. Lee, and H. W. Kim, *J. Nanopart. Res.* **1**, 169 (1999).

<sup>23</sup>W. L. Flower, *Combust. Sci. Technol.* **33**, 17 (1983).

<sup>24</sup>A. Guinier and G. Fournet, *Small Angle Scattering of X-rays* (Wiley, New York, 1955).

<sup>25</sup>R.-J. Roe, *Methods of X-ray and Neutron Scattering in Polymer Science*

- (Oxford University Press, New York, 2000).
- <sup>26</sup>G. G. Long, A. J. Allen, J. Ilavsky, P. R. Jemian, and P. Zschack, in *The ultra-small-angle x-ray scattering instrument on UNICAT at the APS, SRI99* (American Institute of Physics, New York, 1999), pp. 183–187.
- <sup>27</sup>H. K. Kammler, S. E. Pratsinis, P. W. Morrison, Jr., and B. Hemmerling, *Combust. Flame* **128**, 369 (2002).
- <sup>28</sup>R. A. Dobbins and C. M. Megaridis, *Langmuir* **3**, 254 (1987).
- <sup>29</sup>S. Tsantilis, H. K. Kammler, and S. E. Pratsinis, *Chem. Eng. Sci.* **57**, 2139 (2002).
- <sup>30</sup>H. K. Kammler, R. Jossen, P. W. Morrison, Jr., S. E. Pratsinis, and G. Beaucage, *Powder Technol.* **135-136**, 310 (2003).
- <sup>31</sup>A. J. Allen, P. R. Jemian, D. R. Black, H. E. Burdette, R. D. Spal, S. Krueger, and G. G. Long, *Nucl. Instrum. Methods Phys. Res. A* **347**, 487 (1994).
- <sup>32</sup>G. Beaucage, *J. Appl. Crystallogr.* **28**, 717 (1995).
- <sup>33</sup>G. Beaucage, *J. Appl. Crystallogr.* **29**, 134 (1996).
- <sup>34</sup>G. Beaucage, *Phys. Rev. E* **70**, 031401 (2004) (article number for web edition).
- <sup>35</sup>J. Hyeon-Lee, G. Beaucage, S. E. Pratsinis, and S. Vemury, *Langmuir* **14**, 5751 (1998).
- <sup>36</sup>O. Glatter and O. Kratky, *Small-angle X-ray Scattering* (Academic, London, 1982).
- <sup>37</sup>S. K. Friedlander, *Smoke, Dust, and Haze: Fundamentals of Aerosol Dynamics* (Oxford University Press, New York, 2000).
- <sup>38</sup>W. C. Hinds, *Aerosol Technology*, 2nd ed. (Wiley, New York, 1999).
- <sup>39</sup>O. I. Arabi-Katbi, S. E. Pratsinis, P. W. Morrison, Jr., and C. M. Megaridis, *Combust. Flame* **124**, 560 (2001).
- <sup>40</sup>T. T. Kodas and M. J. Hampden-Smith, *Aerosol Processing of Materials* (Wiley-VCH, New York, 1999).
- <sup>41</sup>K. Nakaso, K. Okuyama, M. Shimada, and S. E. Pratsinis, *Chem. Eng. Sci.* **58**, 3327 (2003).
- <sup>42</sup>T. P. Rieker, M. Hindermann-Bischoff, and F. Ehrburger-Dolle, *Langmuir* **16**, 5588 (2000).
- <sup>43</sup>L. Girshick, *J. Chem. Phys.* **107**, 1948 (1997).
- <sup>44</sup>T. Sugimoto, *Monodisperse Particles* (Elsevier, New York, 2001).
- <sup>45</sup>S. Tsantilis, H. Briesen, and S. E. Pratsinis, *Aerosol Sci. Technol.* **34**, 237 (2001).
- <sup>46</sup>C. M. Sorensen, B. Hageman, T. J. Rush, H. Huang, and C. Oh, *Phys. Rev. Lett.* **80**, 1782 (1998).